Field-induced real-space transfer in δ-doped GaAs

H. Kostial, Th. Ihn, P. Kleinert, R. Hey, and M. Asche
Paul Drude Institut für Festkörperelektronik, Hausvogteiplatz 5-7, O-1086 Berlin, Germany

F. Koch
Physik Department der Technischen Universität München, James-Franck-Strasse, D-8046 Garching, Germany
(Received 31 August 1992)

The differential conductivity in various systems of parallel δ layers in GaAs as a function of electric field shows a maximum with subsequent saturation at about 10 V/cm, which manifests itself also in the weak-field magnetoresistivity and Hall effect. The temperature behavior of the peculiarities in the differential conductivity has been studied and compared with results obtained from a balance equation approach to a square-well superlattice taking strict dynamical screening into account. Three effects due to carrier heating in the electric field turn out to be important. A real-space transfer of electrons into the region between the layers and the increase in the electron drift velocity lead to a strong rise of the differential conductivity at lower fields. When heating becomes more and more balanced by the emission of optical phonons the differential conductivity goes through a maximum and saturates.

INTRODUCTION

Advanced epitaxial growth techniques allow the fabrication of δ-doped multilayers in GaAs of high quality. At high δ-doping concentrations neighboring states of impurity electrons strongly overlap, thus leading to the formation of states extended in two dimensions and potential wells along the planes. At low temperatures the diffusive motion of two-dimensional (2D) electrons in these wells determines the zero-field conductivity. The 2D electrons can be transferred into 3D extended states above the barriers by increasing the lattice temperature, by carrier heating in an electric field, or by IR absorption. In contrast to Ref. 1, where the influence of lattice temperature on conductivity was demonstrated, the aim of the present paper is to investigate the field-induced transition from 2D to 3D behavior of the conducting electrons.

The experimental investigations in the dilute metallic limit are compared with numerical simulations. These are based on a two-component model consisting of an arrangement of equidistant square wells, each containing one 2D level and a continuum of extended states above the barriers.

The background for this model shown in Fig. 1 is the result of a self-consistent calculation. Details about these calculations will be published elsewhere.[2] Whereas electrons in lower subbands are bound to single wells, the strong overlap of the wave functions belonging to the uppermost subband leads to the formation of a broad miniband with the consequence of a quasifree mobility in the growth direction.

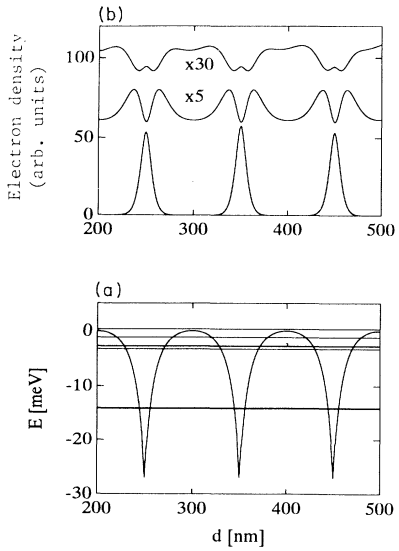

FIG. 1. (a) Conduction-band edge of sample *A*. (b) Electron densities in the zeroth, first, and second subbands.

I. EXPERIMENTS

A. Sample preparation

The δ-doped GaAs samples were grown by molecular-beam epitaxy (MBE) in a Vacuum Generator MBE chamber at 520 °C in a stop-wait-and-go procedure. Sample parameters are shown in Table I. The unintentional background doping was *p* type in the 10^{14}-cm^{-3} range.

B. Experimental results

Figure 2 shows the differential conductivities $\sigma_{\rm diff}(F)$ of samples *A*, *B*, *C*, and *D*. As expected, the decreasing doping concentration (samples *B* to *D*) leads to smaller $\sigma_{\rm diff}(0)$ values. The zero-field conductivities of samples *A* and *B*, however, happen to have nearly the same value in spite of the higher volume doping density of sample *B*.

TABLE I. Sample parameters. The unintentional background doping was p type.

	Sample			
	A	*B*	*C*	*D*
Number of δ layers	8	10	10	12
Sheet-doping concentration (10^{11} cm^{-2})	5	3.4	1.7	1.35
Layer spacing d (nm)	100	17.1	24.3	27.1
Equivalent volume doping (10^{16} cm^{-3})	5	20	7	5
Average distance of dopants in a sheet $\langle a \rangle$ (nm)	14.1	17.1	24.3	27.1
Aspect ratio $r = \langle a \rangle / d$	0.14	1	1	1

This observation can be explained by assuming an enhanced mobility due to ordering the dopants in clearly separated δ layers.

In the weak-field region I the curve for sample A increases more steeply than that for the other samples with the smaller layer spacing. In region II samples A and D, which have the same low effective volume doping density, behave similarly. The higher the effective volume doping density the weaker the conductivity increase in region II. This is due to the smaller mobilities and therefore the less effective carrier heating with increasing doping concentration and also explains the shift of the conductivity maximum towards higher fields. Increasing the field strength beyond the conductivity maximum (region III), only a slightly growing conductivity is observed. Regarding the results of the self-consistent calculation shown above, we suppose that either a mobility increase as a result of carrier heating within the subbands or a real-space transfer into the high-mobility states is responsible for this behavior.

In order to support our interpretation, magnetoresistivity and the Hall effect were measured and will be discussed for sample A. At a magnetic field perpendicular to layers and current (see Fig. 3) one can observe a negative magnetoresistance of about 6% in the zero-electric-field limit, usually referred to as weak localization. It decreases with growing electric-field strength in region II. On the one hand, according to investigations of 2D inversion channels in silicon[3] this can be caused by a reduction of the weak-localization effect due to heating. On the other hand, a growing number of 3D electrons enhances the classical positive magnetoresistivity effect. The magnetoresistance saturates at the same electric-field values where σ_{diff} has its maximum. The saturation value increases with B, as is expected for the classical positive magnetoresistivity effect.

As demonstrated in Fig. 4, an inflection of the slope of R_H is observed at about the same electric fields as for the current. For higher electric fields R_H also saturates.

Since the ratio $n^{(3D)}/n^{(2D)}$ increases with growing lattice temperature, this influence can be used for a more detailed study of the differential conductivity behavior (Fig. 5). The zero-field conductivity clearly reflects the growing percentage of 3D carriers with higher mobility as compared to the 2D electrons. Furthermore the maximum value of the differential conductivity decreases with sample heating and moves towards smaller field values. In regions I and II temperature plays more and more the role of the dominant excitation mechanism compared to the electric field. At high field strengths be-

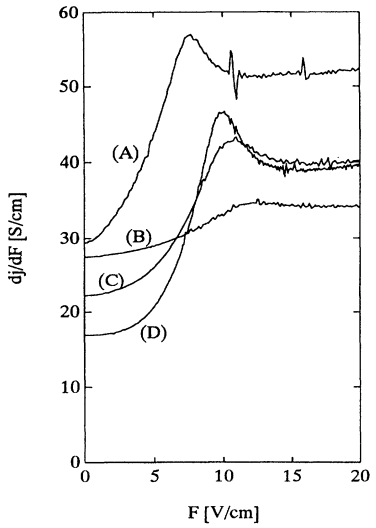

FIG. 2. Differential conductivity of the samples as a function of the electric-field strength at 4.2 K.

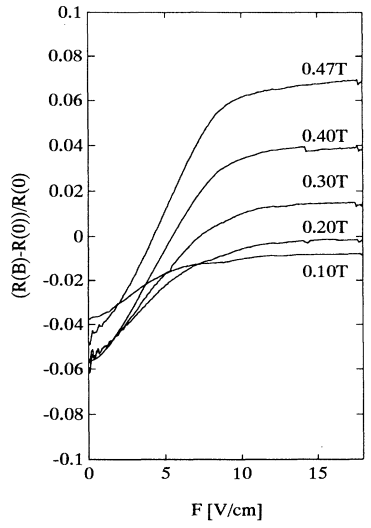

FIG. 3. Magnetoresistance of the sample A as a function of the electric-field strength at 4.2 K and various magnetic fields

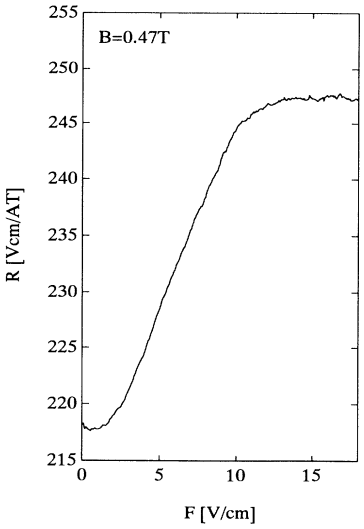

FIG. 4. The Hall constant as a function of the electric field for sample *A*.

longing to region III the temperature is not sufficient to influence the conductivity significantly.

II. THEORETICAL MODEL

Instead of a self-consistent (see Fig. 1) and field-dependent calculation of the potential of the δ-doped layers a rigid square-well superlattice with a width a of the wells and distance d between them is assumed. The energy levels are approximated by one subband in the well and another state close to the barrier edge, representing the extended states in the uppermost subband of the well and the quasifree states above the barrier. We intend to calculate the differential conductivity in this system of two electron subensembles in order to elucidate the effect of carrier heating on the intrasubband drift velocity and on a real-space transfer of the carriers from the well to the interlayer space.

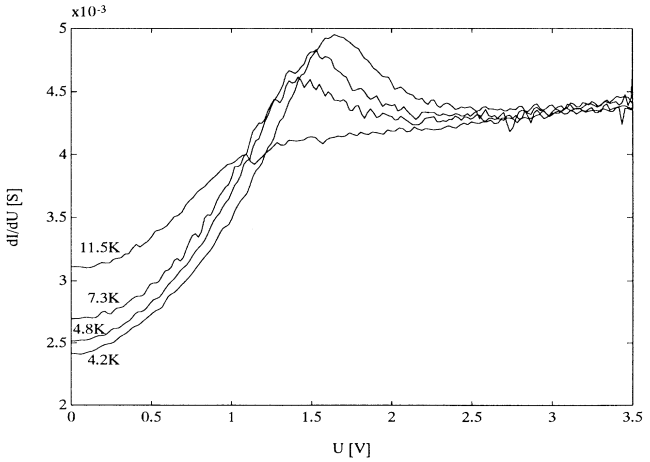

FIG. 5. Temperature dependence of σ_{diff} for sample *A* as a function of the voltage.

In order to obtain numerical conductivity results we start from force and energy balance equations using shifted Fermi-type distributions for the carrier subensembles.[4] The parametrized balance equation approach allows us to choose an initial state which already resembles the major features of the final state, thus making the perturbation theory analysis more effective. Furthermore, the modification of correlation functions by the dynamic screening of the interaction processes can be easily accounted for. This is essential because the dielectric function depends on the drift velocity via the frequency variable and because screening mainly determines impurity-mediated resistivity contributions.

At high carrier concentrations electron-electron scattering can be assumed to be the dominating interaction process allowing the approximation of a Fermi-type distribution function with an electron temperature shifted in the current direction. Whereas the assumption of a T_e^{2D} is well justified for the subsystem of 2D electrons because of their density of 5×10^{11} cm^{-2}, the shift corresponding to a drift of their center of mass is more questionable because of the strong impurity scattering in the layer, which is comparable in strength to the electron-electron collisions with respect to momentum relaxation. With regard to the 3D electrons, at those electric fields for which the real-space transfer sets in (i.e., when only some percent of the carriers are in extended states) the assumption of a shifted Fermi-type distribution is still more crude, since electron-electron collisions are no longer the dominating interaction process compared to phonon emission. However, since the simplicity of such a description by two Fermi gases is advantageous, we try to explain the main experimental features by a numerical simulation within this frame.

The electron temperatures and the drift velocities of the centers of mass are determined by the equations for the energy balance and the force equations, neglecting the scattering between both types of states in comparison to all the other scattering events. On the other hand the scattering between the 2D and 3D subbands reduces the differences between both subsystems, of course, and as a consequence the effects will be overestimated in our calculation. Furthermore, n^{3D}/n^{2D} is assumed as a static ratio. It is determined by the $T_e^{(j)}$ and the Fermi energy E_f resulting from the conservation of the number of electrons, and not by the particle balance equation between the subsystems taking real-space transfer by carrier-carrier collisions and Coulomb scattering on impurities explicitly into account.

The equations for the balance of force and of energy read[4]

$$\begin{aligned} &n_s^{(j)}eF+f(v^{(j)},T_e^{(j)})=0\ , \\ &v^{(j)}f(v^{(j)},T_e^{(j)})+W(v^{(j)},T_e^{(j)})=0\ , \end{aligned} \tag{1}$$

where j refers to quasi-two-dimensional and quasi-three-dimensional contributions. The $v^{(j)}$ are the corresponding components of the drift velocities parallel to the electric field and $T_e^{(j)}$ the electron temperatures. The averaged frictional forces f and energy-transfer rates W result

from impurity, acoustical deformation potential, as well as piezoelectric and polar optical-phonon scattering:

$$f(v^{(j)},T_e^{(j)})=f_i(v^{(j)},T_e^{(j)})+f_{\rm op}(v^{(j)},T_e^{(j)}) +f_{\rm ac}(v^{(j)},T_e^{(j)}) ,$$
$$W(v^{(j)},T_e^{(j)})=W_{\rm op}(v^{(j)},T_e^{(j)})+W_{\rm ac}(v^{(j)},T_e^{(j)}) . \quad (2)$$

The expressions for the superlattice contributions are published in Ref. 5, and those for 3D electrons in Ref. 4. Dynamical screening was accounted for and the 2D density-density correlation function is given, for example, in Ref. 6. As already mentioned, the population of 2D and 3D electronic states is only statically treated. Therefore we obtain the Fermi energy E_f from

$$n_s=2\sum_{\rm q}\frac{1}{e^{(\varepsilon_{\rm q}-E_f)/k_BT_e}+1} +2d\sum_{\rm Q}\frac{1}{e^{(E_{\rm Q}-E_f)/k_BT_e}+1} , \quad (3)$$

where the energy dispersion relations are given by

$$\varepsilon_{\rm q}=\frac{\hbar^2}{2m^*}(q_x^2+q_y^2) ,$$
$$E_{\rm Q}=E_c+\frac{\hbar^2}{2m^*}(q_x^2+q_y^2+q_z^2) , \quad (4)$$

and E_c is the energy separation between the bottom of the 3D bands and the considered quasi-2D energy level.

The numerical procedure is as follows. For a given electron temperature T_e from (3) the Fermi energy E_f is determined. Then from (1) and (2) the drift velocities $v^{(2D)},v^{(3D)}$ and electric-field strengths F are obtained. By interpolation all relevant quantities are referred to a given electric field, and the current density is obtained from

$$J=en^{(2D)}v^{(2D)}+en^{(3D)}v^{(3D)} . \quad (5)$$

With the electron temperatures $T_e^{(2D)}$ and $T_e^{(3D)}$ obtained for the regarded field strength one can start an iteration procedure from (3) and Eqs. (1) and (2) to account for the fact that both electronic subsystems have different electron temperatures. Such a procedure leads to small corrections only at 4.2 K, where the small value of $n^{(3D)}$ is still of minor importance for the determination of the Fermi energy.

III. DISCUSSION OF NUMERICAL RESULTS

The numerical results for the various contributions to f and W are shown in Figs. 6(a) and 6(b), respectively, for the δ-layer impurity concentration $n_s=5\times10^{11}$ cm^{-2}, $d=100$ nm, $a=10$ nm, the energy difference between the ground level and the barrier height $E_c=18$ meV, and the residual bulk doping with $N_{\rm I}=10^{15}$ cm^{-3}. The results are in accordance with the expected influences of the various interaction processes. In the force balance the 2D impurity contribution plays the major role, followed by the 3D impurity and optical-phonon parts. The energy-transfer rates W are dominated by 3D optical

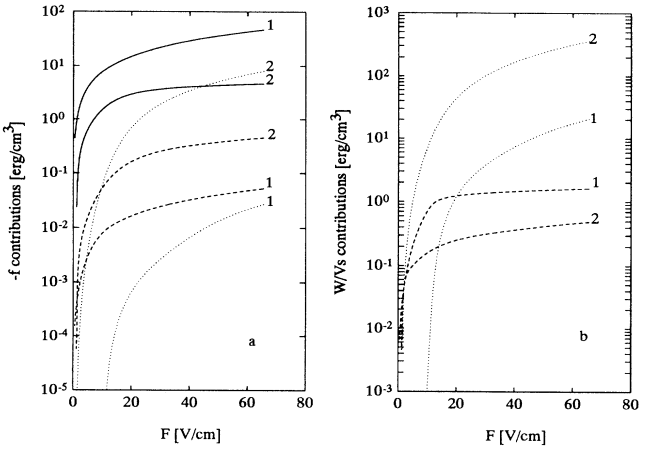

FIG. 6. (a) Friction forces as functions of electric-field strength for momentum relaxation on ionized impurities (solid lines), acoustic phonons as the sum of deformation and piezoelectric scattering contributions (dashed lines), and polar optical phonons (dotted lines). The data for the superlattice approximation are given in the text. (1) and (2) are the 2D and 3D parts, respectively. (b) Energy losses as functions of the electric-field strength.

phonons. Except for very low electric-field strengths acoustical phonons are of minor importance in the balance equations.

The electron temperatures as functions of the electric-field strength F are depicted in Fig. 7. They show a strong increase at relatively weak fields and exhibit a range with almost no temperature increase for the electrons at higher fields. This effect is caused by the strong emission of optical phonons when $k_BT_e^{(3D)}\approx0.1\hbar\omega_0$, balancing a further increase of energy gained by the field. In the considered field region the gain of the quasi-2D electrons is much lower because of the stronger friction force due to impurities.

The field dependence of the carrier densities n^{2D} and n^{3D} are plotted in Fig. 8. An initial rapid rise of n^{3D} with the electric field follows an almost field-independent

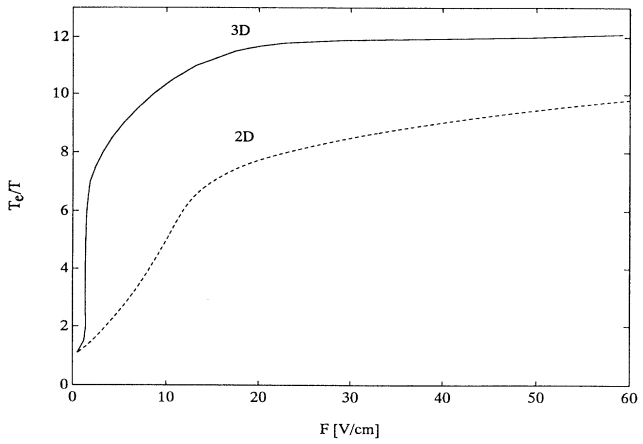

FIG. 7. Electron temperatures vs electric-field strength.

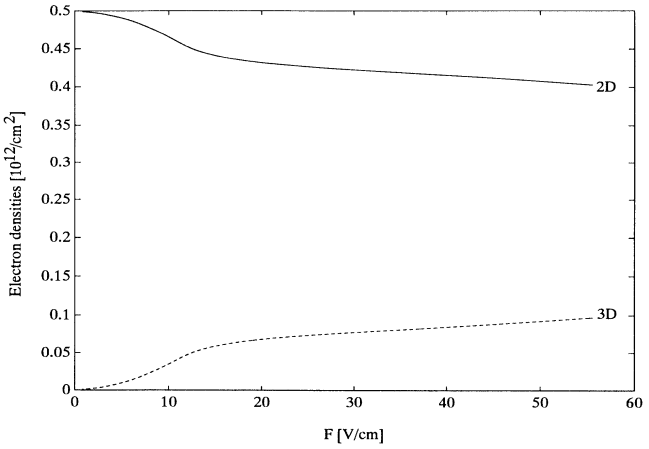

FIG. 8. Field dependence of the 2D and 3D carrier densities.

ratio n^{3D}/n^{2D}, corresponding to the saturation of the electron temperatures in Fig. 7.

The 2D and 3D current contributions and the total current are shown in Fig. 9. Due to their higher mobility at 4.2 K, the electrons in the extended 3D states dominate the current-voltage behavior already at 10 V/cm. The initial rise of the current with growing field strength comes from the excitation of mobile 3D electrons. At higher field strengths the current density increases strongly because of the heating of the 3D electrons. When the dependence of the 3D electron temperature $T_e^{(3D)}$ on the field starts to saturate the current-voltage curve exhibits a sublinear character. Therefore there must be a point of inflection in the current-voltage dependence which gives rise to a maximum in the differential conductivity, as shown in Fig. 10.

In spite of the simplifying assumptions on which the theoretical model is based the data reflect the experimental observation for sample A (Fig. 2) qualitatively well and confirm the interpretation of real-space carrier transfer from the δ layers to the interlayer space. At

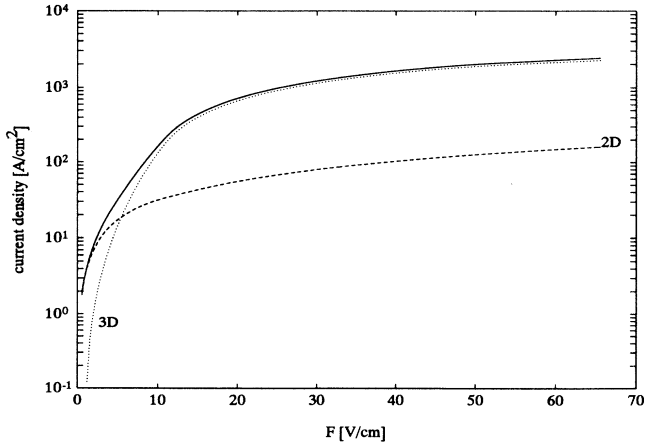

FIG. 9. Current contributions from the 2D and 3D electrons and total current vs electric field.

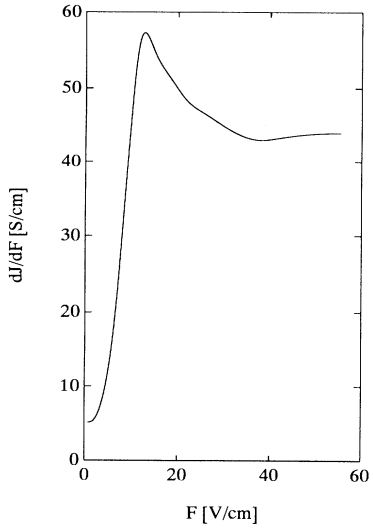

FIG. 10. Differential conductivity dj/dF vs electric-field strength for the parameters of Fig. 5.

fields above a few V/cm, when the contribution of the 3D electrons to the total current dominates, the differential conductivity becomes determined by the influence of carrier heating on their mobility.

At higher lattice temperature (3) has to be replaced by the particle balance equation taking the interaction between 2D and 3D electrons into account. This problem remains to be solved.

CONCLUSION

The peculiarities of the differential conductivity as a function of electric field can be qualitatively explained by the electron heating and its influence on the drift velocities, as well as the transition from 2D to 3D states.

The differential conductivity clearly depends on the local distribution of the dopants. For samples with a large distance between the δ layers in comparison to the average donor distance in the layers the electron transfer from the wells into the space between the layers is strongly pronounced. Therefore the transport behavior is determined by the extended states and the field dependence of the differential conductivity becomes similar to a sample with aspect ratio 1 and the same equivalent volume doping. Its absolute value, however, is significantly higher due to the reduced impurity scattering in the interlayer region.

Comparing samples with aspect ratio 1 the increase of the effective volume concentration weakens the rise of the differential conductivity in the field region below the strong emission of optical phonons, because for fixed electric fields the carriers are less heated due to higher impurity scattering. A self-consistent calculation of the potential under the condition of real-space transfer of heated electrons as well as a dynamic balance between 2D and 3D electrons for higher lattice temperatures requires a more detailed theoretical treatment.

[1]Xiao-mei Feng *et al.*, Surf. Sci. **263**, 147 (1992).
[2]K. Friedland, Th. Ihn, and R. Zimmermand (unpublished).
[3]R. A. Davies, M. J. Uren, and M. Pepper, J. Phys. C **14**, L531 (1981).
[4]X. L. Lei and C. S. Ting, Phys. Rev. B **32**, 1112, (1985).
[5]X. L. Lei and N. J. M. Horing, Solid State Commun. **58**, 235 (1986).
[6]X. L. Lei, J. L. Birman, and C. S. Ting, J. Appl. Phys. **58**, 2270 (1985).